JOURNAL OF SPACECRAFT AND ROCKETS
Vol. 31, No. 2, March–April 1994

Determination of Slender Body Aerodynamics Using Discrete Vortex Methods

G. A. Gebert*
Utah State University, Logan, Utah 84322

Current aerodynamic interest has turned to the study of supermaneuverable fighters and weapon performance when launched in extreme flight conditions. The evaluation of design missile performance requires multiple runs of six degree-of-freedom (6-DOF) simulations, analyzing the missile behavior for a variety of launch and flight conditions. Before wind-tunnel tests, it is necessary to produce the aerodynamic loading of candidate missiles for 6-DOF analyses. Since semi-empirical formulas fail in regions of nonlinear aerodynamics, and solutions to the full Navier-Stokes equations are too costly and time consuming, an alternative method of discrete vortex analysis is re-examined. The present theory examines the three-dimensional nature of the shed vorticity and generalizes previous discrete vortex analyses. Consequently, the results demonstrate relative user independence in determining all slender-body loading at angles of attack from 0 to 70 deg. The rapid calculations of the discrete vortex method makes it a prime candidate for the determinations of high angle-of-attack aerodynamic databases.

Nomenclature

C_m = pitching-moment coefficient
C_N = normal-force coefficient
C_n = yawing-moment coefficient
C_Y = Side-force coefficient
c_1 = Joukowski constant
d = distance along vortex filament to its origin
h = transformed body radius
i = imaginary number, $\sqrt{-1}$
L = reference length
L_b = total body length
M = upstream Mach number
N = normal force
N_v = number of vortices
p = pressure
Re = crossflow Reynolds number based on local body diameter
r = body cross-sectional radius
r_v = perpendicular distance from a point to a vortex line
t = time
U = crossflow plane uniform upstream velocity
U_e = potential velocity at boundary-layer edge
u, v = crossflow plane velocity components in ξ and η directions, respectively
V_∞ = uniform upstream flow velocity
W = complex potential $\Phi + i\Psi$
x, y, z = body-fixed coordinate system
z = crossflow complex variable, $x + iy$
α = mean flow angle of attack
β = compressibility factor, $\sqrt{1 - M_c^2}$
Γ = nascent vortex strength
γ = angle of body surface with respect to x axis
δ = boundary-layer height
ζ = complex position variable, $\xi + i\eta$
θ' = vortex flow angularity
ν = kinematic viscosity
ξ, η = crossflow plane coordinate system
ρ = density
ϕ = velocity potential
ψ = stream function
$\bar{\omega}$ = complex nondimensional crossflow velocity

Subscripts

b = value at missile base
c = crossflow plane properties
cp = center of pressure
e = previous step value
i = i^{th} vortex properties
s = value at body surface
T = total value
∞ = value infinitely far from body
0 = reference quantity

Superscripts

$*$ = intermediate parameter
$\bar{}$ = complex conjugate

Operators

Δ = small quantity, jump across discontinuity
∇ = del
Re{ } = real part
Im{ } = imaginary part

Received Feb. 18, 1992; revision received Jan. 29, 1993; accepted for publication Jan. 29, 1993.

*Assistant Professor, Department of Mechanical and Aerospace Engineering. Member AIAA.

Introduction

BECAUSE of the development of the supermaneuverable fighter, there has been an increased interest in the performance of slender missiles at high angles of attack. Under the supermaneuverable fighter programs, the aircraft are designed to perform controlled maneuvers up to an angle of attack (AOA) of 70 deg at velocities generally below a Mach number of 0.4. Although the aircraft performance is being analyzed in such flight regimes, little is known of the performance of missiles launched during such extreme maneuvers. Missile aerodynamic performance in the high AOA, low Mach number regime is required to understand the missile behavior. Determination of the aerodynamic characteristics of airframes at high incidence to a uniform mean upstream flow poses several difficulties not found at lower AOA. For moderate and high AOA, flow separates on the leeward side of the airframe. At the separation location, the vorticity within the boundary layer ejects into the outer flow. The shed vorticity rolls up into large vortices near the body. For slender bodies at moderate AOA, a pair of symmetric vortices form above the body. At some critical AOA, the vortices become asymmetric. Large side forces result, which can greatly alter the aerodynamic performance of the airframe. In some instances, exper-

iments have shown that the out-of-plane forces are actually larger than the in-plane forces.

Computational fluid dynamics (CFD) methods resulting from a finite differencing of the Navier-Stokes equations and appropriate turbulence models can produce results that agree well with experiments. However, such methods are generally computationally intensive and are currently impractical for the solutions of time-dependent flow and the construction of a database of aerodynamic performance. An alternative method to solving the full Navier-Stokes equations that requires less computer time and is still capable of predicting the out-of-plane as well as the in-plane forces and moments on missile-type bodies is desired.

This paper summarizes and extends a theory for determining the aerodynamics of a missile at AOA up to 70 deg. The methodology is presented for calculating the in-plane as well as the out-of-plane forces and moments. Similar methods of calculating the loads on slender bodies have been presented.[1-6] However, the results relied heavily on empirical data and mathematical assumptions, making the application of the theories questionable when used in the force and moment predictions on arbitrary missile configurations. The present analysis uses potential flow theory together with a general integral boundary layer solver to determine the flowfield and subsequently the forces on an axisymmetric body. The current methodology eliminates all but two arbitrary parameters, and the final solution shows relative insensitivity to values of those parameters.

Potential Flow Model

At moderate and high angles of incidence, the flow on the leeward side of a slender body separates, and vortices are shed from the boundary layer to the outer flow. The shed vorticity can roll up and form large vortices along the leeward side of the missile as shown in Fig. 1. The incoming flow is considered in terms of its axial component $V_\infty \cos\alpha$ and its crossflow component $V_\infty \sin\alpha$, where α is measured as the angle between the body central axis and the upstream uniform velocity V_∞. It is assumed that the crossflow plane is swept uniformly down the length of the body at the rate of the axial flow. The solution to the flow over the body is then calculated by determining the flow around an impulsively starting cylinder of varying size. The results of the time-dependent solution in the crossflow plane are then distributed along the missile body. Although this assumption has been used before, there is no mathematical rationale for it. The elliptic nature of the subsonic flow equations is relaxed, and it is assumed that the downstream flow effects are negligible on the upstream results. The magnitude of this assumption will be shown later.

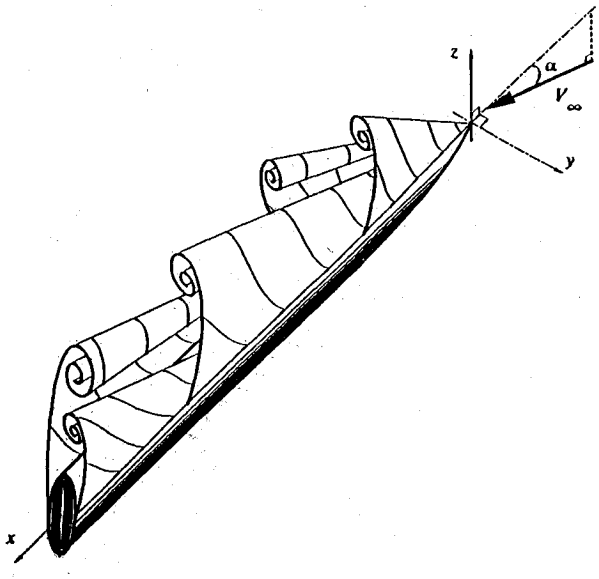

Fig. 1 Schematic of asymmetric vortex development for a slender body at a high angle of attack.

For this analysis, the time-varying flow shown in Fig. 2 is considered. In the crossflow plane, the flow is considered to move from left to right at the velocity $U = V_\infty \sin\alpha$. The streamwise coordinate is ξ, and the perpendicular coordinate is η. For the flow around a cylinder shown schematically in Fig. 2, the stagnation point on the windward surface is located. Integral boundary-layer techniques are marched along the surface to determine the point where the flow separates. For laminar boundary layers, the method of Thwaites[7] is used to calculate the boundary-layer parameters. An estimate is made as to when and if the flow makes a transition to turbulence using a method described by Granville.[8] Turbulent boundary-layer calculations are performed using an entrainment method of Head and Patel.[9] By performing the boundary-layer calculations, the separation point is located along the two-dimensional body surface. At that point, the vorticity that is within the boundary layer is ejected out of the boundary layer to form a small vortex. This process of adding vorticity to the flow happens continuously off both sides of the cylinder. The complex potential W for the flow around a cylinder near a vortex is found using the circle theorem as

$$W = \Phi + i\Psi = U\left(\zeta + \frac{r^2}{\zeta}\right) + \frac{\lambda\Gamma}{2\pi i}\ell n(\zeta - \zeta_j) - \frac{\lambda\Gamma}{2\pi i}\ell n\left(\frac{r^2}{\zeta} - \bar{\zeta}_j\right) \quad (1)$$

where Φ is the velocity potential, Ψ is the stream function, λ is a vortex strength weighting factor that is a function of axial location, and $\zeta_j = \xi_j + i\eta_j$ is the complex position of the vortex center. The complex potential corresponds to a uniform upstream flow around a cylinder together with a vortex located outside the cylinder at ζ_j and an image vortex within the cylinder to preserve the circle as a streamline. For a system of vortices located near the cylinder and a body of changing cross-sectional area, the complex potential becomes the familiar

$$W = U\left(\zeta + \frac{r^2}{\zeta}\right) + \frac{1}{2\pi i}\sum_{j=1}^{N}\lambda_j\Gamma_j\ell n\left(\frac{\zeta^2 - \zeta\zeta_j}{r^2 - \zeta\bar{\zeta}_j}\right) + \frac{\mu}{2\pi}\ell n(\zeta) \quad (2)$$

where μ is the strength of a source located at the center of the cylinder. The strength of the source is dependent on the rate of change of the body radius, which will be discussed later. The complex conjugate of the two-dimensional velocity field is then found by taking the derivative of Eq. (2) with respect to ζ, which gives

$$\frac{dW}{d\zeta} = u - iv = U\left(1 - \frac{r^2}{\zeta^2}\right) + \frac{1}{2\pi i}\sum_{j=1}^{N}\lambda_j\Gamma_j \times\left(\frac{2\zeta - \zeta_j}{\zeta^2 - \zeta\zeta_j} + \frac{\bar{\zeta}_j}{r^2 - \zeta\bar{\zeta}_j}\right) + \frac{\mu}{2\pi\zeta} \quad (3)$$

Equation (3) represents the velocity field in the two-dimensional crossflow plane. Quantities yet to be determined are the shed vortex strengths $\lambda_j\Gamma_j$ and the source strength μ. The flowfield changes in time since the radius r is changing and the vortices are continuously shed and convected by the flow. Drawing the analogy between the time-varying crossflow plane flow and the spatially varying three-dimensional flow over the slender body gives the relation

$$x = V_\infty \cos(\alpha)t \quad (4)$$

where, as shown in Fig. 1, x is the axial coordinate along the missile and is, positive aft, y is out the side of the body, and z is up. The y and z coordinates, respectively, correspond to the η and ξ coordinates in the crossflow plane (Fig. 2). The crossflow component of the upstream velocity is then $U = V_\infty \sin\alpha$. The coordinate x is set equal to zero at the

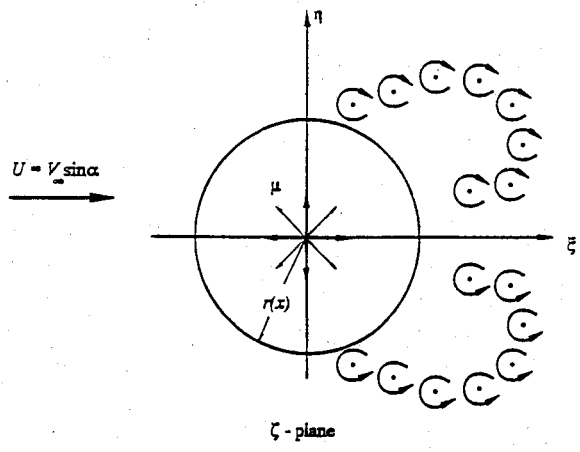

Fig. 2 Schematic of nascent vortex shedding at a typical section in the crossflow, ζ plane.

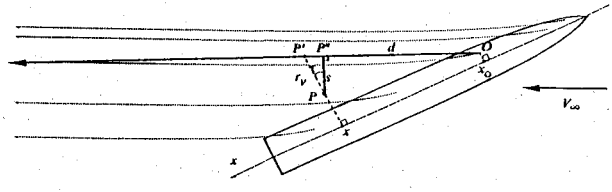

Fig. 3 Schematic of the semi-infinite vortex filament system trailing a slender body at a high angle of attack.

missile nose tip. The radius of the missile is a known function of axial location x and therefore can be transformed into a function of time.

The source term in Eq. (3) must have the proper strength to insure impermeability of the body surface as the radius changes. In the time-developing crossflow plane, a point located on the body surface has the magnitude $|\zeta| = r$. The radial velocity associated with the source for a given point located on the surface is $\mu/(2\pi r)$. For a given increment in time Δt, there is an associated change in the radius Δr. The source must have the proper strength to push the flow away from the origin Δr over a given length of time Δt for points located on the surface. Thus, $\mu\Delta t/(2\pi r) = \Delta r$. Taking the limit and substituting Eq. (4) for time gives the result

$$\frac{\mu}{2\pi} = r\frac{\mathrm{d}r}{\mathrm{d}x}V_\infty\cos(\alpha) \tag{5}$$

Vorticity is introduced into the potential flow as the boundary layer separates and the vorticity within the boundary layer is ejected outward. The location of the separation point is found by using an integral boundary-layer solver. The actual details of determining the separation location will not be discussed here but are given in other references.[7-9] Once the separation point is known, the vorticity within the boundary layer at that point can be calculated by noting that the vorticity flux through any two-dimensional boundary layer is given as[10]

$$\frac{\mathrm{d}\Gamma}{\mathrm{d}t} = \int_0^\delta V\cdot(\nabla\times V)\,\mathrm{d}y' = \int_0^\delta u'\frac{\mathrm{d}u'}{\mathrm{d}y'}\mathrm{d}y' = \frac{U_e^2}{2} \tag{6}$$

where V is the velocity vector, y' is a coordinate measured perpendicular to the surface, and u' is the velocity component parallel to the surface. The value of U_e is given by the outer, potential flow solution. Using Eq. (4) and solving Eq. (6) for the $\mathrm{d}\Gamma$ term gives

$$\mathrm{d}\Gamma = \pm\frac{U_e^2}{2}\frac{\mathrm{d}x}{V_\infty\cos(\alpha)} \tag{7}$$

Thus, for an incremental distance along the body axis $\mathrm{d}x$, the amount of vorticity $\mathrm{d}\Gamma$ given in Eq. (7) is ejected into the flow at the location of each boundary-layer separation point. The exact location of the shed vortex is determined by making the velocity at the separation location vanish. Hence, the sum of the velocity induced by the new shed nascent vortex together with the velocity induced by the previous vortices, the body source, and the upstream flow equals zero at the separation point. The sign of the vorticity depends on the rotation direction of the vortex.

A two-dimensional vortex as shown in Fig. 2 is assumed to be a cross-sectional cut of vortex filament that extends from $-\infty$ to $+\infty$. This is not truly the case in marching the flow down the axisymmetric body. In the three-dimensional steady flow problem, each vortex filament starts at a specific x location and extends to infinity downstream. The strength of the semi-infinite vortex filament is somewhat less than the strength predicted by Eq. (7). Previous researchers, at this point, have introduced a factor to reduce the strength of the shed vortex. The value of the parameter was chosen so as to achieve reasonable agreement with experiments. In subsonic flows, a typical value is 0.6. A physical explanation in the weighting factor exists in the fact that an infinite vortex line model is being used to model the semi-infinite vortex filaments. The Biot-Savart law can be used to calculate the actual velocity induced at the point due to the semi-infinite vortex line.

Figure 3 shows a single vortex filament that was created at the axial location x_0. Because of viscosity and impingement on the body surface, the filament is assumed to start at x_0 and extend downstream to infinity. In this approximation, the vortex is assumed to be straight. The Biot-Savart law is readily applied to the vortex filament to give the velocity at an arbitrary point P as

$$U_P = \frac{\Gamma}{4\pi r_v\cos(\tau)}\left(1+\frac{d}{\sqrt{d^2+s^2}}\right) \tag{8}$$

where r_v is the distance from P to the point where the filament intersects the crossflow plane P', s is the distance from P to the closest point along the filament P'', d is the distance from P'' to the origin of the vortex line O, and the angle τ is defined as $\cos^{-1}(s/r_v)$. Note that very near the starting location of the vortex the factor multiplying the vortex strength is nearly 0.5, but further downstream the multiplication factor approaches 1.0.

In addition to this three-dimensional effect, viscosity plays a role in diffusing the vortex and altering its induced velocity. Equation (3) yields a singularity at the center of each vortex filament. To remove the singularity, the well-known viscous vortex solution[11] is considered, which makes the velocity at the point P

$$U_P = \frac{\Gamma}{4\pi r_v\cos(\tau)}\left(1+\frac{d}{\sqrt{d^2+s^2}}\right)\left\{1-\exp\left[\frac{r_v^2V_\infty^2\sin(2\alpha)Re}{8\nu(x-x_0)}\right]\right\} \tag{9}$$

where Re is the Reynolds number of the crossflow at the point where the vortex was created, x is the axial position of the point P, and x_0 is the axial location where the vortex line originated. By this formula, the strength of the filament changes along the vortex line. For the present analysis, the strength of the filament is calculated at each section. The strength of the entire semi-infinite vortex line is assumed to be constant and equal to the calculated strength at the given section.

By comparing Eq. (9) with the vortex term of Eq. (3), it is seen that the value of λ_j is given as

$$\lambda_j = \frac{1+\epsilon_j}{2\cos(\tau)}\left(1+\frac{d}{\sqrt{d^2+s^2}}\right)\left\{1-\exp\left[\frac{r_v^2V_\infty^2\sin(2\alpha)Re_j}{8\nu(x-x_0)}\right]\right\} \tag{10}$$

where Re_j is the crossflow Reynolds number corresponding to the creation of the jth vortex, and a disturbance parameter ϵ_j has been introduced to disturb the flow slightly at given cross sections. The total velocity field is given by Eqs. (3), (5), (7), and (10) as

$$u - iv = V_\infty \sin(\alpha)\bar{\omega} \tag{11a}$$

where

$$\bar{\omega} = \left(1 - \frac{r^2}{\zeta^2}\right) + \frac{1}{2\pi i}\sum_{j=1}^{N}\lambda_j\Gamma_j\left(\frac{2\zeta - \zeta_j}{\zeta^2 - \zeta\zeta_j} + \frac{\bar{\zeta}_j}{r^2 - \zeta\bar{\zeta}_j}\right) + r\frac{dr}{dx}\frac{1}{\tan(\alpha)}\frac{1}{\zeta} \tag{11b}$$

where λ_j is given by Eq. (10), and

$$\Gamma_j = \pm \tfrac{1}{2}\tan(\alpha)\bar{\omega}_e^2\Delta x \tag{11c}$$

where the value of $\bar{\omega}_e$ is given by Eq. (11b) evaluated at the separation point at the previous step. Note that the calculation of the velocity field has been written at discrete axial positions. Rather than continuous shedding of vorticity, discrete vortices (nascent vortices) are introduced into the flow at given intervals.

For a known axisymmetric shape, AOA, and flow velocity, Eqs. (11a–11c) define the potential incompressible flowfield

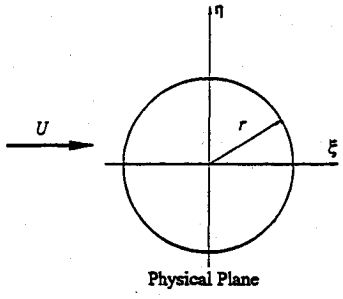

Fig. 4a Typical cross section of the slender body in compressible flow, ζ plane.

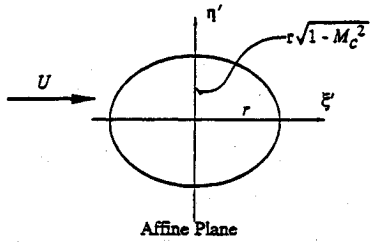

Fig. 4b Affinely transformed cross section of the slender body in incompressible flow, ζ' plane.

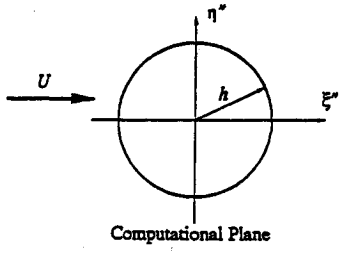

Fig. 4c Conformal mapped cross section of the slender body in incompressible flow, ζ'' plane.

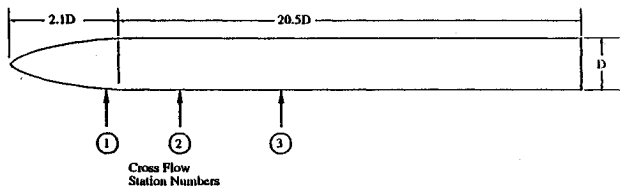

Fig. 5 Schematic of a typical pointed slender body with a 2.1D nose and 20.5D afterbody.

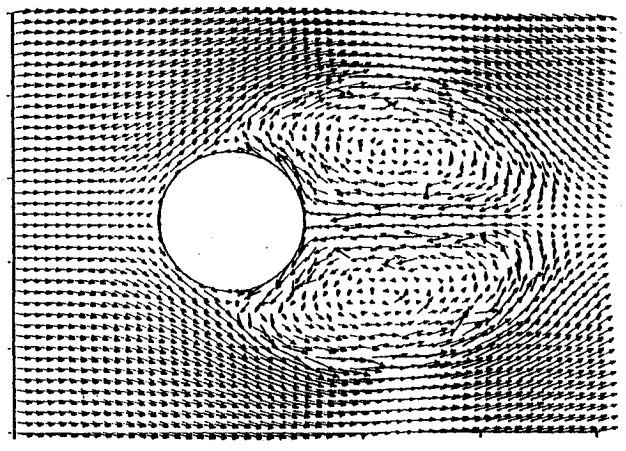

Fig. 6 Vector plot of the crossflow field of a typical slender body with no flow perturbation, missile station 3.

around the slender body. Each vortex is convected by the flow and allowed to interact with the flow and other vortices as the flow develops. At each section, this flowfield is used by the boundary-layer solver to determine the separation location and the strength of the new shed vortices. In this manner, the flow is marched down the body from the nose.

Method of Solution

Using the equations derived, the flow around the slender body can be calculated. The missile body is divided into a large finite number of circular disks. The height of each disk is Δx. The flow changes more rapidly for the smaller radii near the nose. A similarity analysis indicates that the Δx along the body should be $\Delta x = 2r\Delta x_b/d$, where d is the base diameter of the body, and Δx_b is the body increment at the base. An additional similarity analysis indicates that the value of Δx_b is dependent on the angle of attack such that $\Delta x_b \tan(\alpha) = \text{const}$.

Initially, at the first cylindrical disk, the potential velocity of a uniform flow around a cylinder is calculated. The boundary-layer analysis is performed to determine the location of the separation points. At each separation point a discrete nascent vortex is shed with strength given by Eq. (11c). The solution is then advanced to the next disk. The boundary-layer analysis is performed using the velocity defined in Eqs. (11a–11c), and the separation points are located. New nascent vortices are shed at those locations. The positions of the vortices are calculated using a second-order Runge-Kutta method as the velocity field convects the vortices along. Each vortex induces no velocity on itself.

As the solution is marched down the body, the normal and side forces per unit length are then calculated at each cylindrical disk section by summing the pressures around each cross section. Thus, at each section the normal and side-force coefficients are simply given by

$$\Delta C_N = \frac{\Delta x r}{\tfrac{1}{2}\rho V_\infty^2 \pi r_0^2}\int_0^{2\pi}(p_s - p_\infty)\cos(\theta)\, d\theta \tag{12a}$$

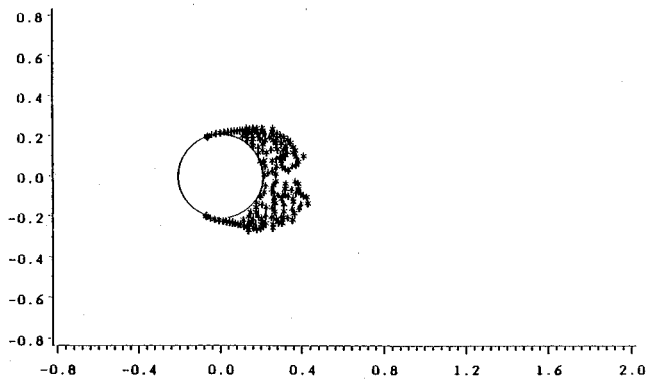

Fig. 7 Nascent vortex development on a typical slender body with flow perturbation, missile station 1.

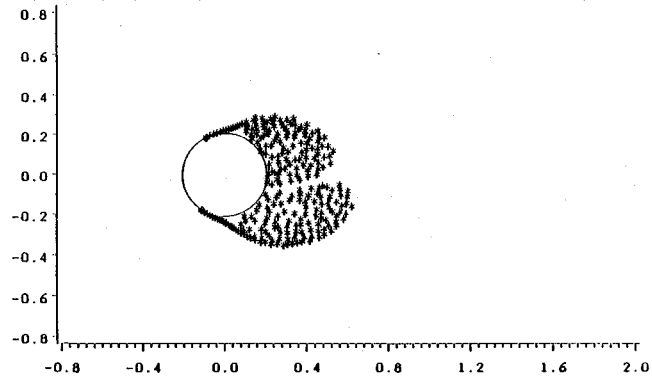

Fig. 8 Nascent vortex development on a typical slender body with flow perturbation, missile station 2.

and

$$\Delta C_Y = \frac{\Delta x r}{\tfrac{1}{2}\rho V_\infty^2 \pi r_0^2}\int_0^{2\pi} (p_s - p_\infty)\sin(\theta)\, d\theta \qquad (12b)$$

where ΔC_N and ΔC_Y are the section normal and side force, respectively.

The pressure difference needed in Eqs. (12a) and (12b) is found by employing the Bernoulli equation. It is noted that the flow solution, as derived, is time dependent, which is then transformed to an equivalent x dependence, and therefore the unsteady Bernoulli equation states

$$p_s - p_\infty = \tfrac{1}{2}\rho V_\infty^2\left[1 - \left(\frac{V_s}{V_\infty}\right)^2 - \frac{1}{V_\infty^2}\frac{\partial}{\partial t}(\Phi_s - \Phi_\infty)\right] \qquad (13)$$

where the flow is considered incompressible and irrotational. The velocity potential is given as the real part of Eq. (2). Thus, by noting Eq. (4), the appropriate derivative of the velocity potential is

$$\frac{\partial \Phi}{\partial t} = Re\left(\frac{\partial W}{\partial x}\frac{\partial x}{\partial t}\right) = V_\infty \cos(\alpha) Re\left(V_\infty \sin(\alpha)\frac{2r}{\zeta}\frac{dr}{dx}\right.$$
$$+ \frac{1}{2\pi i}\sum_{j=1}^{N}\left\{\frac{\partial(\lambda_j\Gamma_j)}{\partial x}\ell n\left(\frac{\zeta^2 - \zeta\zeta_j}{r^2 - \zeta\bar{\zeta}_j}\right) - \lambda_j\Gamma_j\left[\frac{\partial \zeta_j}{\partial x}\frac{1}{\zeta - \zeta_j}\right.\right.$$
$$\left.\left. + \frac{2r(\partial r/\partial x) - (\partial \bar{\zeta}_j/\partial x)}{r^2 - \zeta\bar{\zeta}_j}\right]\right\} + \frac{\partial}{\partial x}\left(r\frac{\partial r}{\partial x}\right)\frac{\ell n(\zeta)}{\tan(\alpha)}\Bigg) \qquad (14)$$

From Eq. (14) it is seen that a logarithmic singularity exists at infinity. Hence, in evaluating for the pressure difference, the results can only be known within an additive constant. The constant is integrated out when the total body forces and moments are calculated. Equation (14) can be evaluated for values of ζ along the body surface, and the value of the derivative at infinity can be taken to be zero. Hence Eq. (13) can be evaluated for any point along the surface, and the subsequent forces can be evaluated. The total forces are merely the sum of the incremental forces, and the pitching moment C_m and yawing moment C_n are given as the weighted sums of the normal-force and side-force coefficients along the body.

As the solution is marched down the missile, and the forces and moments are calculated at each section. It is important to note that the transformation between the spatial flow and the time-developing flow given in Eq. (4) is based on observation. Since the flow is subsonic, the actual flow at each point is dependent on the flow of every other point within the field. Thus the transformation used here must be viewed as an approximate solution to the equations governing the flow.

Compressibility Effects

Thus far, all equations derived have been developed for incompressible flow by finding solutions to Laplace's equation and using superposition to create the flow. An attempt is made to account for compressibility effects by applying Gothert's rule.[12] The rule strictly applies to slender bodies that can be treated with small perturbation theory in flows where viscous effects are not important. This is not the case here. However, the use of this rule is in line with the approximate nature of the study, and it has been used successfully by previous researchers.[13]

Gothert's rule relates compressible flow to an incompressible flow over a slightly different geometry. If C_N and C_Y represent the normal and side forces on a given section of a body in incompressible flow, and C_N' and C_Y' are the normal

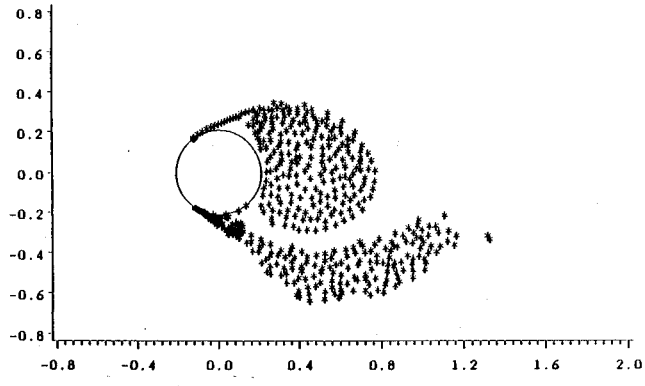

Fig. 9 Nascent vortex development on a typical slender body with flow perturbation, missile station 3.

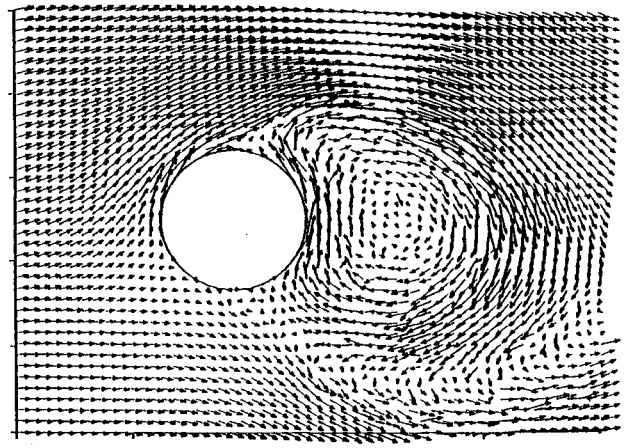

Fig. 10 Vector plot of the crossflow field of a typical slender body with flow perturbation, missile station 3.

and side forces in the corresponding compressible flow, then Gothert showed the relationship between the flows gives

$$C_Y' = \frac{C_Y}{\beta^2} \quad \text{and} \quad C_N' = \frac{C_N}{\beta^3} \tag{15}$$

The relation holds only if a specific affine transformation between the two geometries exists.

The compressible flow in the crossflow plane around a right-circular cylinder of radius r corresponds to an affinely transformed incompressible flow around an ellipse. Figure 4a shows the compressible flow around a circle. The affinely transformed, corresponding, incompressible flow around an ellipse is shown in Fig. 4b. The ellipse has a semi-major axis r in the direction of the upstream flow, and semi-minor axis βr perpendicular to the flow. Figure 4a is the complex ζ plane, and Fig. 4b is the complex ζ' plane. If the incompressible flow around the ellipse shown in Fig. 4b is calculated, and the forces are calculated, then the forces in the compressible flow plane are known by Eq. (15).

The incompressible flow around the ellipse can be transformed into the incompressible flow around another circle of radius h shown in Fig. 4c by means of a Joukowski-type transformation, whereas

$$\zeta' = \zeta'' + \frac{r^2 M_c^2}{4\zeta''} \quad \text{and} \quad \zeta'' = \tfrac{1}{2}\left(\zeta' \pm \sqrt{\zeta'^2 - r^2 M_c^2}\right) \tag{16}$$

The plus sign in Eq. (16) is chosen when $\mathrm{Re}\{\zeta'\} \geq 0$, and the $-$ sign when $\mathrm{Re}\{\zeta'\} < 0$. The transformation is valid only for subsonic crossflows. The radius of the transformed circle is $h = r(1+\beta)/2$.

Hence, for the compressible flow around a circle of radius r, the incompressible flow around a circle of radius h is calculated by means of Eqs. (11a–11c) where the radius $r(x)$ is replaced by $h(x)$. The flow is then conformally mapped to the flow around an ellipse. The forces and moments can be calculated by integrating the pressure on the ellipse in incompressible flow. It is noted that, for a complex potential W defined in the ζ' plane, the velocity in the ζ' plane is found simply as

$$(u - iv)_{\zeta' \text{plane}} = \frac{dW}{d\zeta'} = \frac{dW}{d\zeta''}\left(\frac{1}{d\zeta'/d\zeta''}\right) = \frac{dW}{d\zeta''}\left[\frac{1}{1 - (r^2 M_c^2/4\zeta''^2)}\right] \tag{17}$$

where $dW/d\zeta''$ is defined by Eqs. (11a–11c).

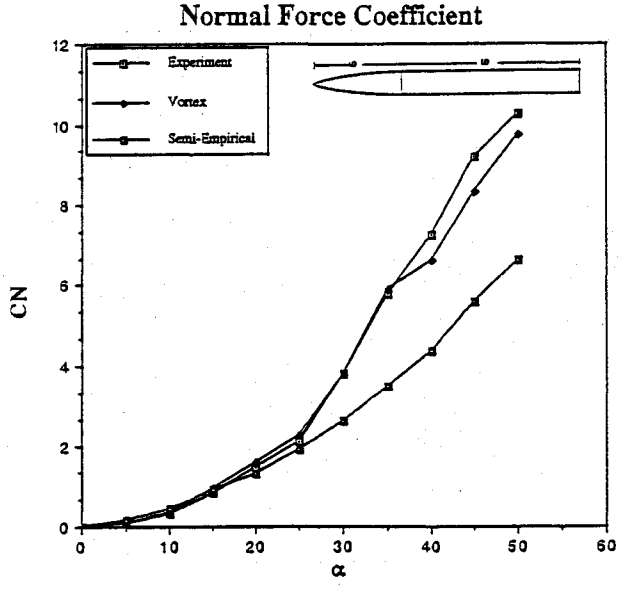

Fig. 11 Comparison of normal force coefficients on a 4*D* nose, 8*D* body missile at mach 0.5.

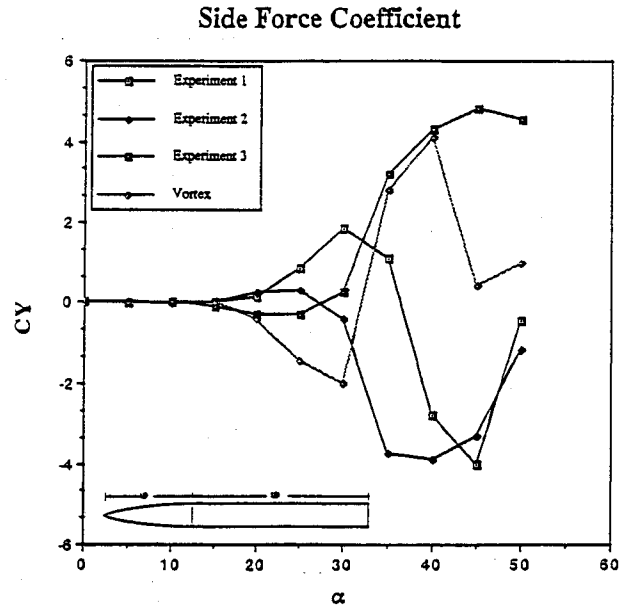

Fig. 12 Comparison of side-force coefficients on a 4*D* nose, 8*D* body missile at mach 0.5.

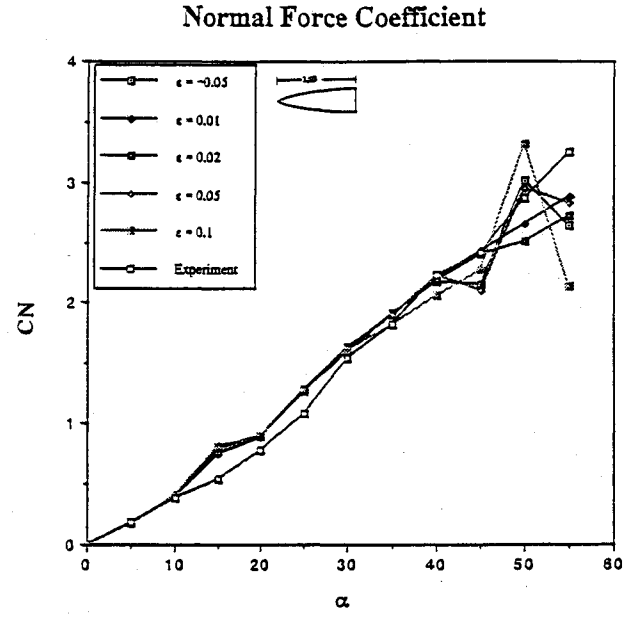

Fig. 13 Comparison of the estimated values of the normal-force coefficient on a 3.5*D* ogive nose for various flow perturbation values.

The boundary-layer analysis is then performed in the ζ' plane by calculating the corresponding velocity and geometry at each point on the surface. Separation is then calculated and the corresponding separation angle is determined in the ζ' plane to locate the nascent vortex.

Now all necessary equations to determine the compressible separated flow around a pointed missile have been derived. The solution requires a computer to calculate the flowfield and resulting forces. It was found that a rather small step size was required for stable solutions, which resulted in the tracking of thousands or even tens of thousands of nascent vortices. The computer code can be run in a matter of several days on microcomputers or in about 10 h on a VAX 8550. However, the code vectorized extremely well, and results on the Cray YMP seldom took longer than 20 min, and usually results were achieved in less than 3 min.

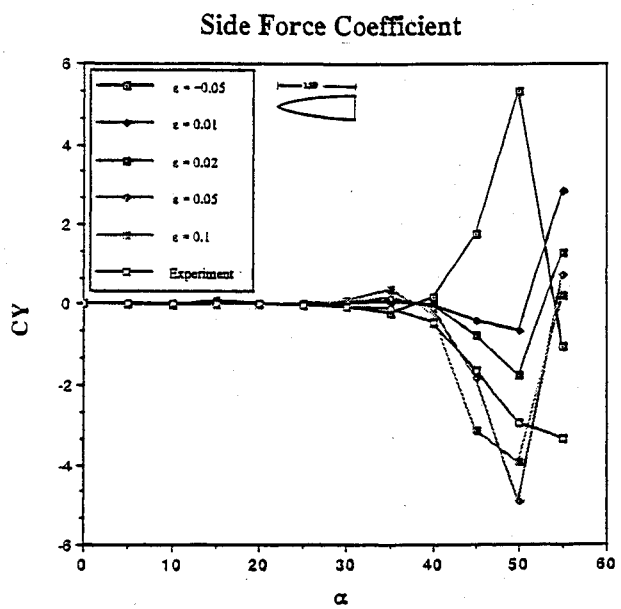

Fig. 14 Comparison of the estimated values of the side-force coefficient on a 3.5*D* ogive nose for various flow perturbation values.

Discussion of the Results

Several slender-body configurations have been run to determine the aerodynamics. The results were compared against experimental data to determine the validity of the method. Additionally, perturbation parameters were varied to determine the sensitivity of the results to the magnitude of those parameters.

Figure 5 shows a schematic of a typical slender body having a pointed ogive nose of length 2.1 diameters and an afterbody length of 20.5 diameters. On this particular missile configuration, several angle-of-attack and Mach numbers were run. Positions of the shed nascent vortices and the entire flowfield were output at several missile stations as shown in the figure. Missile station 1 is located at the end of the nose section of the missile. Station 2 is 1/6 of the total body length measured from the nose, and station 3 is the midsection of the body.

A vector diagram of the velocity flowfield at station 3 is shown in Fig. 6. The angle of attack of the body is 40 deg, and the Mach number is 0.3. The flow, in this cross-sectional cut, moves from the left to the right. In this figure, the flow is undisturbed. The value of ϵ_j in Eq. (10) is set identically equal to 0.0 for all shed vortices. Symmetric large counter-rotating vortices behind the missile are clearly shown. In the separated region, there is significant flow reversal, and the vortices have grown to a large size. Although the equations predict such a solution, physically it is intuitively unreasonable to expect such a perfectly symmetric solution at the given geometry and angle of attack of the body. Small disturbances in the upstream flow and imperfections in the body would lead to an asymmetric solution.

An asymmetric solution can be introduced into the equations in several ways. The boundary-layer separation points or the roll orientation of the upstream AOA can be perturbed. However, for this analysis, the strength of vorticity shed on one side of the body is slightly perturbed near the nose tip of the missile. This is accomplished by multiplying the calculated vortex strength [Eq. (10)] by some value near but not equal to unity. The flow is perturbed in this manner for some small distance near the nose tip. The two additional parameters (perturbation value ϵ_j and the distance of flow perturbed δ_d) were varied to determine the sensitivity of the results on the perturbation values.

In Figs. 7-9, the shed vortices are plotted again at missile stations 1, 2, and 3, respectively, for the slender body shown in Fig. 5. In this case, the flow is perturbed by setting the value of ϵ_j equal to 0.05 for the vortices shed on one side of the body ($\epsilon_j = 0.0$ on the other side) for a distance down from the nose tip of $\delta_d = 0.01L_b$ or 1% of the total nose length. Note that from this small perturbation at this high angle of attack, the asymmetry grows at each axial location. A slight difference in the leeward vortices is evident at missile station 1. However, at missile station 2, the size and position of the vortices clearly show asymmetry, and at station 3 a tremendous difference in the vortices exists. Note also that in Fig. 9 there is a concentration of counterclockwise vorticity forming near the body. This vorticity will tend to push the large clockwise vortex away from the body, thus forming the beginning of a von Kármán vortex street. It is noted that the crossflow Reynolds number is consistent with experimental Reynolds numbers where a vortex street is observed.

A vector diagram of the crossflow field at missile station 3 is shown in Fig. 10. Clearly, the beginning of a vortex street is shown, and large asymmetry in the flowfield is apparent. It should be restated that this large asymmetry occurred as the result of a very small perturbation in the value of the shed vorticity near the nose tip. At this angle of attack, a large von Kármán vortex street develops behind the body. However, at smaller angles of attack, the perturbations tend to die away, and a symmetry vortex shedding occurs.

The in-plane and out-of-plane forces were calculated on a slender body having a nose length of 4.0 diameters and an afterbody length of 8.0 diameters. The results were then compared against experimental values generated by Wardlaw.[14] For this case the angle of attack was varied from 0 to 50 deg. The Mach number is 0.5. The shed vortex strengths on a single side of the body were again perturbed with $\epsilon_j = 0.05$ and $\delta_d = 0.01L_b$ near the nose tip. Figure 11 shows a comparison of the normal-force coefficient as predicted by the present theory and the high angle-of-attack formula of Jorgensen[15] with the experimental results. Note that the present theory does a reasonably good job of predicting the normal force throughout the entire angle-of-attack regime. Jorgensen's formula predicts significantly lower values at the larger angles of incidence.

The side-force coefficients C_Y for this flow are shown in Fig. 12. In this figure, three different experimental curves are given for three different roll configurations. Significant scatter is shown in the experimental data even though the missile is supposedly symmetric. Note that the present theory reasonably predicts the magnitude of the out-of-plane force and

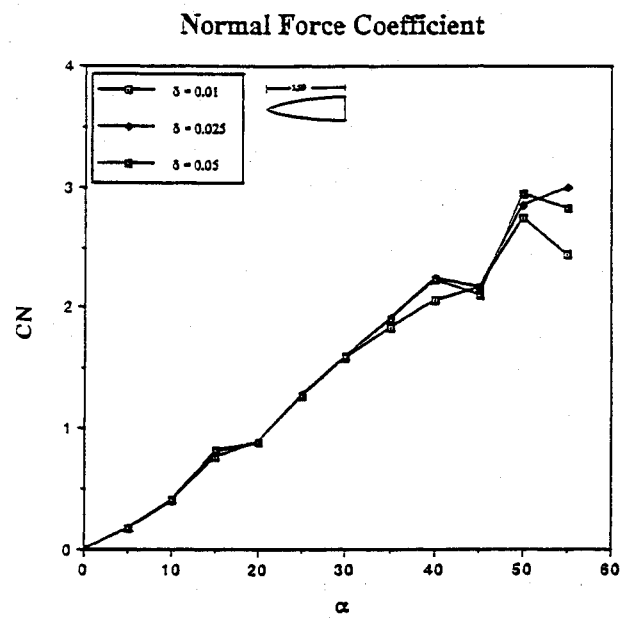

Fig. 15 Comparison of the estimated values of the normal-force coefficient on a 3.5*D* ogive nose for various flow perturbation distances.

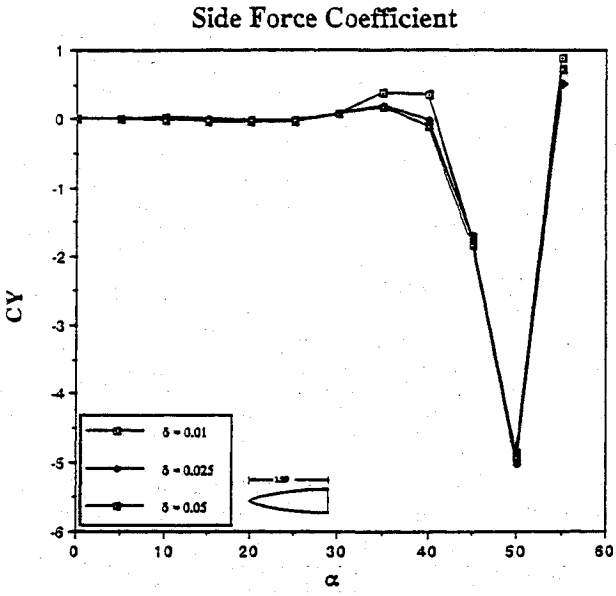

Fig. 16 Comparison of the estimated values of the side-force coefficient on a 3.5*D* ogive nose for various flow perturbation distances.

picks up the sign change of the force throughout the angle-of-attack regime.

The effect of the perturbation values were analyzed, and the results are shown in Figs. 13–16. The figures show the normal-force and side-force coefficients on a 3.5-diam ogive nose. The results are compared with the experimental results of Roos and Kegelman.[16] The base diameter of the nose is 3 in., and the Mach number of the flow is 0.0868.

Figures 13 and 14 show the effect of the perturbing constant. For these cases, the value of the shed vortex strengths on one side of the missile are modified by letting ϵ_j equal -0.05, 0.01, 0.02, 0.05, and 0.1. The flow is perturbed at the nose tip for a distance of only 1% of the total nose length, $\delta_d = 0.01L_b$. The normal-force coefficients presented in Fig. 13 display good agreement between all of the different perturbation values and the experimental results. The side-force coefficients illustrated in Fig. 14 show considerable differences in the calculated values. However, the general magnitudes at the given angles of attack show good agreement with each other and the experimental results. These results exhibit reasonable independence between the net force calculations and the initial perturbation parameter.

The effect of the amount of the flow perturbed are examined in Figs. 15 and 16. Again, a 3.5-diam ogive nose at Mach number 0.0868 was examined. For these results, the flow was perturbed at the nose tip by setting $\epsilon_j = 0.05$ for distances along the body of 1, 2.5, and 5% of the total nose length, $\delta_d = 0.01L_b$, $0.025L_b$, and $0.05L_b$, respectively. Throughout most of the angle-of-attack regime, both the normal-force and side-force coefficients show little difference in the results due to changes in the perturbation distances. As was the case in Figs. 13 and 14, little dependence exists between the final results and the perturbation value.

Conclusions

Discrete vortex methods have been used and studied by researchers for many years. The methods capture the essential large scale physics of the flow and rapidly compute the net aerodynamics of given bodies. The swift response of the methods gives them a distinct advantage over more computer-time-intensive methods. By employing a boundary-layer solver and analyzing the semi-infinite nature of each vortex filament, the present method removes all but two arbitrary parameters necessary to perturb the solution.

The analysis has demonstrated reasonable independence of the net force calculations on the magnitude of the perturbation parameters. Several different slender-body geometries were examined, and all showed good agreement with experimental results.

Computation times are small when compared with solution times for the full Navier-Stokes equations. It was determined that stable solutions require fine spacing of the cross sections along the missile. This results in the tracking of thousands or even tens of thousands of nascent vortices. It can take a considerable length of time on a standard computer. However, the code algorithm vectorizes well, and solutions on a Cray Y-MP rarely take longer than 20 min. Thus, for flow analyses that require multiple aerodynamic solutions, such as the creation of aerodynamic databases or aeroelastic analysis, the present application of discrete vortex methods gives a viable means of total aerodynamic predictions.

Acknowledgments

This work was supported by Sverdrup Technology, Inc., through a grant from the U.S. Air Force Armament Lab at Eglin Air Force Base in Florida. The author wishes to thank the individuals at Sverdrup and in the Armament Lab for all assistance provided.

References

[1]Deffenbaugh, F. D., and Marshall, F. J., "Time Development of the Flow About an Impulsively Started Cylinder," *AIAA Journal,* Vol. 14, No. 7, 1976, pp. 908–913.

[2]Thomsom, K. D., and Morrison, D. F., "The Spacing, Position, and Strength of Vortices in the Wake of Slender, Cylindrical Bodies at Large Incidence," *Journal of Fluid Mechanics,* Vol. 50, Pt. 4, 1977, pp. 751–783.

[3]Wardlaw, A. B., "Prediction of Normal Force, Pitching Moment, and Yawing Force on Bodies of Revolution at Angles of Attack up to 50 Degrees Using a Concentrated Vortex Flow-Field Model," Naval Ordinance Lab., NOL TR 73-209, Silver Spring, MD, Oct. 1973.

[4]Angelucci, S. B., "A Multivortex Method for Axisymmetric Bodies at Angle of Attack," *Journal of Aircraft,* Vol. 8, No. 12, 1971, pp. 959–966.

[5]Marshall, F. J., and Deffenbaugh, F. D., "Separated Flow over Bodies of Revolution Using an Unsteady Discrete-Vorticity Cross Wake; Part I—Theory and Applications," NASA CR-2414, June 1974.

[6]Mendenhall, M. R., and Lesieutre, D. J., "Prediction of Vortex Shedding from Circular and Noncircular Bodies in Subsonic Flow," NASA CR 4037, Jan. 1987.

[7]Thwaites, B., "Approximate Calculations of the Laminar Boundary Layer," *Aeronautical Quarterly,* Vol. 1, No. 4, 1949, pp. 245–280.

[8]Granville, P. S., "The Calculation of Viscous Drag of Bodies of Revolution," Navy Dept., David Taylor Model Basin, Rept. 849, Washington, DC, July 1953.

[9]Head, M. R., and Patel, V. C., "Improved Entrainment Method for Calculating Turbulent Boundary Layer Development," NASA Ames Research Center, ARC R&M3643, Moffett Field, CA, Feb. 1969.

[10]Laird, A. D. K., "Eddy Formation Behind Circular Cylinders," *Journal of the Hydraulic Division, Proceedings of the American Society of Civil Engineers,* Vol. 21, No. 2, 1971, pp. 111–116.

[11]Schaefer, J. W., and Eskinazi, S., "The Vortex Street Generated in a Viscous Fluid," *Journal of Mechanics,* Vol. 6, Pt. 2, 1959, pp. 241–260.

[12]Schlichting, H., *Boundary Layer Analysis,* McGraw-Hill, New York, 1979, pp. 25–28.

[13]Wardlaw, A. B., "Multivortex Model of Asymmetric Shedding on Slender Bodies at High Angles of Attack," AIAA Paper 75-123, Jan. 1975.

[14]Wardlaw, A. B., "High Angle of Attack Missile Aerodynamics," AGARD LS-98, Feb. 1979, pp. 5.1–5.53.

[15]Jorgensen, L. H., "Prediction of Static Aerodynamic Characteristics for Space-Shuttle-Like and Other Bodies at Angles of Attack from 0° to 180°," NASA TN D-6996, Jan. 1973.

[16]Roos, F. W., and Kegelman, J. T., "Aerodynamic Characteristics of Three Generic Forebodies at High Angles of Attack," AIAA Paper 91-0275, Jan. 1991.